General Parametrization of Persisting Long-Range Nanoscale Phenomena in Force Measurements Emerging under Ambient Conditions

Francesco Lo Iacono,[†,‡] Nicolas Bologna,[†,‡] Maria Vittoria Diamanti,[‡] Yun-Hsiang Chang,[†] Sergio Santos,[†] and Matteo Chiesa*[,†]

[†]Laboratory for Energy and NanoScience (LENS), Institute Center for Future Energy (iFES), Masdar Institute of Science and Technology, Abu Dhabi, UAE

[‡]Dipartimento di Chimica, Materiali ed Ingegneria Chimica "G. Natta", Politecnico di Milano, Milano, Italy

Received: March 17, 2015
Revised: April 25, 2015

Corresponding Author
*E-mail mchiesa@masdar.ac.ae (M.C.).

1. INTRODUCTION

The atomic force microscope (AFM) has been employed over the past decades to probe material properties and phenomena with nm and sub-nm spatial resolution[1−3] and with sub-nm and sub-Å vertical resolution.[4] Information however is vastly based on contrast directly arising from variations in the experimental observables, i.e., deflection,[5] amplitude,[6,7] phase,[8] frequency,[9] or other,[10] that is presented without further processing. Variations in observables arise from variations in material properties,[11] topography, or an interplay between the two.[11,12] Ultimately, a general aim is to obtain contrast via observables and then transform them via suitable models to build contrast maps based on physically relevant properties.[13,14] In this respect, the AFM is reaching a new state of maturity in terms of quantification of material properties of complex systems,[13−18] i.e., Young modulus, viscoelasticity, sample deformation, etc., and even atoms[19] via the selection of suitable models when imaging under appropriate environments.[13,14] Nevertheless, the availability and success of contact mechanics models have arguably led to the vast majority of works dealing with quantification to focus on contact (repulsive) forces and the related Young modulus, viscoelasticity, and mechanical deformation.[13,14] Furthermore, when dealing with forces other than those involved in the region of mechanical contact, it is typically the force as a function of distance alone that is directly reported.[20,21] Here we deal with the nonmechanical part of the force that persist fractions of nm and several nm above the surface. We refer to these nonmechanical forces as long-range forces for simplicity and generality. There are many complexities involved with long-range forces in ambient conditions such as the coexistence of forces with different physical origin, i.e., London dispersion, electrostatic, magnetic, capillary, and so on.[22] In this work we propose that rather than focusing on the physical origin of the force, force profiles and other emerging nanoscale phenomena are suitably parametrized, thus providing quantitative information about samples even in the absence of suitable models or a full understanding of the underlying physics,[22] i.e., whether one or another long-range force should be accounted for.

2. EXPERIMENTAL SECTION

2.1. Materials. Glass, silica, sapphire, mica, HOPG (graphite), gold, platinum, HEMA (2-hydroxyethyl methacrylate), and PFDA (1*H*,1*H*,2*H*,2*H*-perfluorodecyl acrylate) have been employed as model systems. Mica and HOPG are a first group of materials here. These samples are atomically flat, have the advantage of allowing exfoliation, and can be employed as hydrophilic and hydrophobic model systems. A second group of materials in this study consists of oxide materials presenting nanoscale homogeneity, i.e., glass, silica, and sapphire surfaces. A third group consists of gold and platinum surfaces. These are transition metals for which contaminants might rapidly

adhere,[23,24] i.e., minutes, onto their surfaces once submitted to ambient conditions. The fourth and last group consists of HEMA (hydrophilic) and PFDA (hydrophobic) surfaces. This choice of polymers provide us data from hydrophilic and hydrophobic polymer surfaces[25,26] onto which nanoscale water films form (HEMA) and do not form (PFDA) with time. Neither HEMA nor PFDA was submitted to annealing.

Two treatments here are identified as (1) annealing the samples for hours, 2−3 h, while in vacuum conditions at temperatures above the boiling point of water, ∼130−150 °C, and (2) aging the samples in ambient conditions for days and at relative humidity ∼70−80% (RH) as done elsewhere.[27] When submitted to treatment 1, the samples are termed annealed samples, and when submitted to treatment 2, the samples are termed aged samples for simplicity. The two treatments are also termed annealed and aged throughout. Experimental data for the annealed samples (treatment 1) was collected within 1 h after annealing. For the mica and graphite samples the annealed treatment was found to be equivalent to exfoliating (not shown). The rationale behind the choice of treatments involves the fact that, when exposed to ambient conditions, a material's surface may undergo rapid changes. This is arguably one of the great challenges to robustly and reproducibly mapping nanoscale properties under ambient conditions.[23,28−30] By submitting our samples to these two extremes, we account for such variability. At least 50 sampling points were collected for each sample (and/or treatment), and mean values are reported here throughout.

2.2. Force Reconstruction. The governing equation of motion in amplitude modulation (AM) AFM is typically modeled with the use of a point-mass oscillator[31]

$$m\frac{d^2z}{dt^2} + \frac{m\omega_0}{Q}\frac{dz}{dt} + kz = F_{ts} + F_D \tag{1}$$

where z is the instantaneous position of the tip relative to its unperturbed equilibrium position, z_c is the tip−sample separation, k is the spring constant, Q is the quality factor due to dissipation with the medium, ω_0 is natural frequency, the effective mass is $m = k/\omega_0^2$, $F_D = F_0\cos(\omega t)$ is the external driving force, and ω is the drive frequency ($\omega \approx \omega_0$).[31] Cantilever with $Q \approx 500$, $f_0 \approx 300$ kHz ($\omega_0 \equiv 2\pi f_0$), and $k \approx 40$ N/m (Olympus AC160TS) have been employed here throughout. The tip−sample distance d can be written as $d = z_c + z$. Then, the Sader−Jarvis−Katan formalism[32,33] can be employed to reconstruct the conservative part of the force in terms of the minimum distance of approach d_m where $d_m \approx z_c - A$

$$F_{ts}(d_m) = 2k\int_{u=d_m}^{u=\infty}\left[\left(1 + \frac{A^{1/2}(u)}{8\sqrt{\pi(u-d_m)}}\right)\Omega(u) - \frac{A^{3/2}(u)}{\sqrt{2(u-d_m)}}\frac{d\Omega(u)}{du}\right]du \tag{2}$$

and

$$\Omega(d_m) = \left[1 + \frac{A_0}{QA}\cos(\Phi(d_m))\right]^{1/2} - 1 \tag{3}$$

where $\Omega(d_m)$ is the normalized frequency shift, A_0 is the free (unperturbed) amplitude, and Φ is the phase lag. In AM AFM A_0, $A(z_c)$, $\Phi(z_c)$, and z_c are experimental observables and suffice to employ this formalism with the constraint that in AM AFM A/A_0 should remain close to 1.[34] Since the tip−sample distance d coincides with d_m in this formalism,[35] from now on $d_m \equiv d$. Higher modes are neglected by employing (1) alone and higher harmonics are further neglected in the derivation of (2) and (3).[36,37] In the context of AM AFM, expressions 2 and 3 have been already subjected to very complex forces in simulations,[34,38] including dissipation, and have been shown to involve very small errors, i.e., <1−2%, in the attractive regime which is the subject matter of this work. In summary, from the formalism in (2) and (3), the experimental raw vectors $A(z_c)$, $\Phi(z_c)$, and z_c, the expression $d \approx z_c - A$, and the calibration[39] of k, Q, and ω_0, the force as a function of distance $F_{ts}(d)$ has been recovered.

2.3. Parametrization and Metrics. Figure 1a shows a cartoon of a force profile where the method to quantify the metric dF_{AD} is illustrated. F_{AD} coincides with minima in force and is identified with the force of adhesion. The metric dF_{AD} is defined as the distance for which $F_{ts}(d) \leq 0.8F_{AD}$, and it is employed to detect or identify "plateaus in the attractive part of the force". The factor 0.8 has been arbitrarily chosen, since we experimentally found that, with this numeric coefficient, dF_{AD} is not affected by the noise level of the force reconstruction algorithm.[40] Figure 1b shows a cartoon of the expected behavior of the oscillation amplitude A as a function of cantilever separation z_c, i.e., amplitude curves, as hypothesized by the simulations conducted by Barcons et al. In particular, it is expected that, even with the use of relatively small free amplitudes, i.e., $A_0 < 2$−4 nm, the curves presents local minima and local maxima in A. It should also be noted that a region of negative slope in A connects local minima and maxima. This local maxima and minima in A, and the region of negative slope in A, represent a distinctive feature of amplitude curves that is investigated in this work. A specific distance is here parametrized with the use of the metric dAW defined as the z_c distance between a reference amplitude A_{ref} and local maxima in A. AW stands for amplitude width. The main constraint is that A_{ref} should be sufficiently small to allow observing local minima and local maxima in A but large enough to prevent tip blunting. Here we have chosen $A_{ref} \approx 0.5$ nm throughout. When local minima and local maxima in A are not observed, we define dAW = 0. We define a third metric dd_m as shown in the cartoon of Figure 1c. This third metric is defined as $dd_m = D_M - D_m$ and corresponds to the range of distances d of nonzero tip−sample interaction, i.e., $|F_{ts}| \geq 0$. A reference value is also employed here to compute dd_m. A maximum distance D_M is

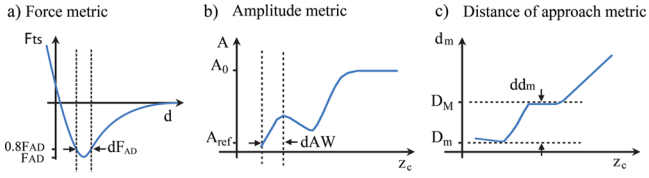

Figure 1. (a) Cartoon of a force profile or force F_{ts} as a function of distance, illustrating how the metric dF_{AD} is defined. (b) Cartoon of the behavior of the oscillation amplitude A with decreasing cantilever separation z_c where the method to define the metric dAW is illustrated. (c) Cartoon illustrating how the minimum distance of approach d_m as a function of separation z_c can be computed via the expression $d_m = z_c - A$. The method to define the metric dd_m rests upon the definition of D_M and D_m, i.e., maximum and minimum distances where the interaction is nonzero.

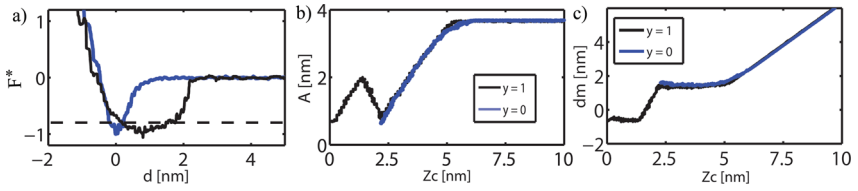

Figure 2. (a) Representative differences in force profiles found experimentally in this work. The examples correspond to cleaved mica (blue lines) and aged sapphire (black lines). The forces have been normalized F^* with the absolute of the adhesion force F_{AD}. The horizontal dashed line corresponds to the threshold for the force metric dF_{AD}, i.e., $0.8F_{AD}$. (b) Corresponding amplitude A versus cantilever separation z_c. The characteristic local maxima and minima is found ($y = 0$) only for the sapphire sample (black lines). (c) Corresponding minimum distance of approach d_m as a function of separation z_c.

defined as the distance for which d_m first deviates by 0.2 nm from a straight line (Figure 1c). Again, this threshold has been chosen to avoid noise artifacts. The second reference point D_m is defined as absolute minima in d_m. The result is illustrated in Figure 1c. Finally, in order to collect data for force reconstruction and the force metric, the free amplitudes were set to $A_0 \approx 15-25$ nm. When collecting data for amplitude (amplitude metric) and distance (distance metric) the free amplitudes were set to $A_0 \approx 2-4$ nm. Finally, from a physical point of view the dF_{AD} metric (force metric) parametrizes the extension of the attractive well, and it is the most general metric here since it applies to any force measurement. The dAW and dd_m metrics (amplitude and distance metrics, respectively) are more restrictive in that they apply to experimental observables in dynamic atomic force microscopy only. From a physical point of view the dAW metric parametrizes the extension of a secondary region where positive slope in amplitude is observed. A main aim here is to relate this metric to dF_{AD} since dAW is computationally low cost and such relationship would also provide physical grounds for the interpretation of this phenomenon, i.e., this region of positive slope in amplitude. Physically, the dd_m metric is arguably more intuitive than the dAW metric since it parametrizes the decay length of the attractive forces, and it is also computationally low cost. A main aim here is to relate this third metric to dAW and dF_{AD}, thus providing physical insight into the physics of these two last metric (dAW and dd_m) via the extension of the attractive well (dF_{AD}).

2.4. Physical Significance of the Three Metrics. The three proposed metrics carry physical significance as follows. First, the distance dF_{AD} can be employed to quantify how persistent large attractive forces are in ambient conditions. Other similar metrics could be defined, such as $dF_{AD} = \alpha F_{AD}$ where α is a parameter that can vary from 0 to 1. By varying α from 0 to 1 any arbitrary force profile can be fully parametrized and quantified. However, for simplicity, and because of the possible relationship that we discuss here between dF_{AD} and the two other parameters, we focus on $\alpha = 0.8$ only to parametrize force profiles. Second, dAW is a metric that provides information about the different tip−surface distances that can be explored via the two regions with positive amplitude decay in Figure 1b. Third, the dd_m metric provides information about the tip−sample distances that can be effectively explored while imaging and also their range of action. In the Results section we show that the three metrics, and therefore possibly the physics controlling the three metrics, are related.

3. RESULTS AND DISCUSSION

An example of the different phenomena observed in terms of force profiles (Figure 2a), amplitude decay (Figure 2b), and minimum distance of approach d_m (Figure 2c) is shown in Figure 2. The force F_{ts} has been normalized throughout, and it is written as F^*. The data in Figure 2 correspond to experiments carried out on freshly cleaved (treatment 1) mica (blue lines) and aged (treatment 2) sapphire (black lines). A horizontal line defines the cutoff for the force metric dF_{AD}, i.e., $0.8F_{AD}$. The values corresponding to this Figure are $dF_{AD} \approx 0.4$ and 1.6 nm, respectively. The corresponding amplitude data in Figure 2b show that maxima in A are only found for the sapphire sample (black lines). For the mica sample on the other hand, the amplitude decays almost linearly with decreasing z_c throughout. This allows us to classify the data according to the presence or absence of the feature illustrated in Figure 1b and experimentally observed in Figure 2b, namely, the presence or absence of local minima and maxima in A. The presence of this feature is from now on defined as $y = 1$ and the absence as $y = 0$. The corresponding distance of approach data is shown in Figure 2c.

Logistic regression was carried out with the use of experimental data (more than 800 data points in total) from the 16 samples (treatments 1 and 2 included) in order to find thresholds in dF_{AD} and dd_m for which $y = 1$. The standard functions optimset and fminunc from Matlab[41] were employed to find the coefficients. The hypotheses are written in terms of the sigmoid function as $h_\theta(dF_{AD})$ and $h_\theta(dd_m)$ for dF_{AD} and dd_m, respectively

$$h_\theta(dF_{AD}) = \frac{1}{1 + e^{17-34dF_{AD}}} \quad (4)$$

$$h_\theta(dd_m) = \frac{1}{1 + e^{28-22dd_m}} \quad (5)$$

The interpretation of (4) and (5) is that the probability of $y = 1$, i.e., observing local minima and maxima in the amplitude curve, is $P(y = 1) = h_\theta(dF_{AD})$ and $h_\theta(dd_m)$ for dF_{AD} and dd_m, respectively. Cutoff values can be defined when $P(y = 1) = 0.5$ and are found to be 0.5 and 1.3 nm respectively for dF_{AD} and dd_m. The implication is that local maxima and minima in A, such as that in Figures 1b and 2b (black lines), will not be seen in amplitude curves when $dF_{AD} < 0.5$ nm or $dd_m < 1.3$ nm. The sigmoid functions (dashed blue lines) in (4) and (5) are plotted in Figure 3 as a function of dF_{AD} (Figure 3a) and dd_m (Figure 3b), respectively. Filled circles and outlined squares correspond to experimental data. We note that $y = 0$ was found only for the annealed (treatment 1) mica and graphite samples and the PFDA sample. For all other samples and/or treatments $y = 1$ and $dF_{AD} > 0.5$ nm. These results indicate that plateaus in the attractive part of the force are a general characteristic of surfaces exposed to the ambient environment. Regarding dd_m, the results in Figure 3b further indicate that long-range

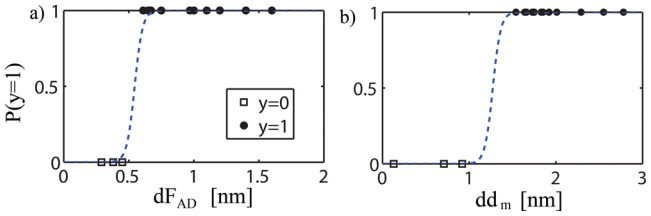

Figure 3. Sigmoid functions (dashed blue lines) found by employing logistic regression with the use of the experimental data sets for (a) dF_{AD} and (b) dd_m. Open squares represent the absence of the local maxima and minima in A (y = 0), while closed circles stand for the presence (y = 1).

attractive forces persist for distances larger than 1 nm. In terms of the work carried out by Santos et al. and Wastl et al. and with regards to high resolution imaging under ambient conditions, the implication is that it is necessary to overcome attractive forces that are significant in magnitude for distances larger than 1 nm before reaching the mechanical contact region under ambient conditions. This is in agreement with their findings.

It is worth recalling that it is not-necessary to recover the tip−sample force with computationally costly expressions such as (2) and (3) in order to quantify dAW or dd_m. Therefore, besides providing insight into the relationship between the dynamics of the cantilever, i.e., dAW and dd_m, and the actual force profile, i.e., dF_{AD}, dependence between the metrics is interesting from a computational point of view. Since linear relationships are simple and desirable, linear regression has been employed to obtain simple models with the use of the polyfit function in Matlab to obtain (all metrics in nm)

$$dF_{AD} = 0.45dd_m + 0.11 \quad (6)$$

$$dF_{AD} = 0.56dWA + 0.37 \quad (7)$$

$$dd_m = 1.18dWA + 0.66 \quad (8)$$

returning coefficients of determination of the polyfit function were RR = 0.62, 0.59, and 0.85, respectively. Scatter diagrams are shown in Figure 4 (triangles for experimental data, blue lines for linear regression, and dashed blue lines for the respective confidence interval at 95%). While (6) and (7) are potential candidates to reduce computational costs, (8) is the best linear model. The data also indicate that the null test hypothesis of zero slope for the three expressions (6)−(8) can be rejected (p-value ≪0.05 on all counts) according to the standard test statistic (t distribution). The physically relevant implication is that variations in any of the three metrics dd_m, dAW, and dF_{AD} lead to significantly variations in the others, i.e., larger plateaus imply larger long-range interaction distances dd_m and larger amplitudes for which the second region with positive slope can be employed for imaging dAW. The estimates for the slopes, standard deviations SD, and the respective standard errors or confidence intervals CI and p values are given in Table 1.

Results so far have been restricted to the use of tips which, according to the critical amplitude method,[42,43] were sharp with tip radius R < 5 nm. In particular, Barcons et al. and Santos et al.[44] discussed that the appearance of the minima and maxima in amplitude as in Figures 1b and 2b, i.e., y = 1 in Figure 3, was dependent on the sharpness of the tips in their experiments. This potential relationship is next discussed with the use of logistic regression as done above in Figure 3. The critical amplitude method was employed to characterize the radii of

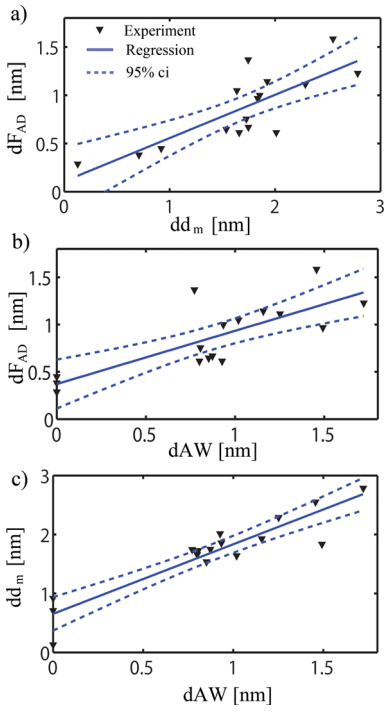

Figure 4. Scatter diagram for (a) dd_m versus dF_{AD}, (b) dAW versus dF_{AD}, and (c) dAW versus dd_m. Linear model (blue lines), 95% confidence interval for the linear model (dashed blue lines), experimental data points (filled triangles) are shown.

Table 1. Estimated Values, Standard Deviations, Standard Errors, or Inferences Based on t Distributions (Confidence Interval and p-Value) for the Slopes in Eqs 6 to 8 and Figure 4[a]

	estimate (slope)	SD (slope)	95% CI (slope)	p-value (slope)
[dd_m, dF_{AD}]	0.45	0.09	[0.25−0.64]	0
[dAW, dF_{AD}]	0.56	0.12	[0.31−0.82]	0
[dAW,dd_m]	1.18	0.13	[0.90, 1.46]	0

[a] p-values are given as 0 because they are orders of magnitude smaller than 0.05.

tips *in situ*. The critical amplitude A_c is a direct experimental observable, and it is identified with the minimum free amplitude A_0 required to observe transitions between force regimes in amplitude and phase distance curves. The relationship $R = 4.5(A_c)^{1.1}$ has been employed here to characterize R for all samples and treatments while employing AC160TS cantilevers from Olympus. In the data up to Figure 4 only tips for which A_c < 7 nm have been employed ensuring that R < 5 nm. Since the hypothesis of Barcons et al. is that y = 1 (with the same meaning as in Figure 3) if and only if the tip is sharp, a range of tip radii were employed to collect data. For this purpose tips were submitted to imaging in the repulsive regime with values of free amplitude close to A_c, in order to broaden them and obtain a given desired value. Similar procedures have been proposed in the literature.[45−47] In the experiments conducted to produce the data for Figures 5 and 6 tips values were $R \approx$ 3−40 nm.

First, Figure 5 shows data representative of the data sets for $R \approx$ 3−4 nm (black lines), R = 7−8 nm (gray squares), and $R \approx$ 40 nm (blue triangles) while employing $A_0 \approx$ 3.5 nm as in Figure 2b,c. The sample in Figure 5 is aged (treatment 2)

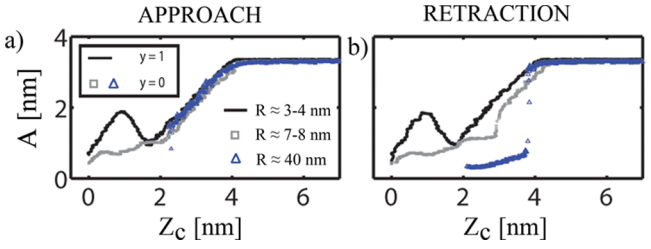

Figure 5. Experimental examples of amplitude A versus separation z_c curves for $R \approx 3-4$, 7–8, and 40 nm during cantilever (a) approach and (b) retraction, respectively. Only with the sharpest tips could the dAW ($y = 1$) feature be observed, indicating the potential of this footprint for *in situ* tip radius discriminant for the sharpest tips.

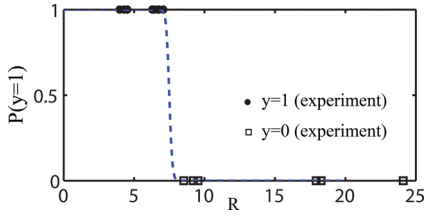

Figure 6. Sigmoid function (dashed blue lines) found by employing logistic regression with the use of the experimental data sets for dAW ($y = 1$ for dAW > 0 and $y = 0$ for dAW = 0) and a range of R. Open squares stand for $y = 0$ while closed circles stand for $y = 1$ as in Figure 3.

sapphire, but similar results could be obtained with other samples except for PFDA (not shown) provided the samples were aged (treatment 2). Approach and retraction data are shown in Figures 5a and 5b, respectively. Local minima and local maxima in amplitude A, as in the illustration in Figure 1b and in the experimental in Figure 2b, are only observed for $R \approx 3-4$ nm (black lines). At very large values of R, $R \approx 40$ nm (blue triangles), the tip gets trapped on approach and retraction. At intermediate values $R = 7-8$ nm (gray squares) the amplitude decays but not linearly. The conclusion is that $y = 1$ (dAW > 0) is obtained only when tips are sharp, implying that the presence of the dAW footprint ($y = 1$) can be employed for rapid determination of whether tips are sharp. Again, this exemplifies the potential use of metrics to quantify phenomena that can lead to useful relationships even without knowledge of the underlying physics.

Next, experimental data from 23 tips (AC160TS from Olympus) have been used to perform logistic regression. The aim is to find a relationship between the presence ($y = 1$ or dAW > 0 as in Figure 3) and absence ($y = 0$ or dAW = 0 as in Figure 3) of local minima and maxima in A and tip radius R. The sample was aged (treatment 2) graphite. The hypothesis is written as $h_\theta(R)$, and the expression is found to be (employing standard Matlab functions as before)

$$h_\theta(R) = \frac{1}{1 + e^{-75+10R}} \tag{9}$$

where, again, $h_\theta(R)$ is identified as the probability function of observing local maxima and minima in A, i.e., $y = 1$. The experimental data points employed for $y = 1$ (black dots) and $y = 0$ (open squares) and the expression in (9) (dashed blue lines) are shown in Figure 6. The critical value of R is found to be $R \approx 7.5$ nm. These results are in agreement with Figure 5 and the discussion above and with the reports of Barcons et al. and Santos et al.

4. CONCLUSIONS

In summary, we have discussed the potential of defining metrics to quantify phenomena and parametrize force profiles that can lead to useful relationships even without deep knowledge of the underlying physics and therefore without the need of a suitable physical model. We have probed a broad set of samples and, with the use of our first metric, we have showed that plateaus in the attractive part of the force are a general characteristic of nanoscale surface forces when surfaces are exposed to the ambient environment. We have further shown that by suitably defining metrics, relationships can be found that can be exploited for useful applications. In particular, we have defined a metric to parametrize and quantify phenomena that can be used to discriminate between sharp, i.e., 7–8 nm or less in radii, and blunt tips. In summary, the parametrization and methods here will pave the way to discriminating between nanoscale phenomena without the necessity of employing suitable and relevant physical models. Thus, this work and future parametrization however could also assist to develop physical models.

Notes

Author Contributions

F.L.I. and N.B. contributed equally.

The authors declare no competing financial interest.

ACKNOWLEDGMENTS

We thank Chia-Yun Lai for helping us edit the manuscript and for useful comments.

REFERENCES

(1) Giessibl, F. J. AFM's Path to Atomic Resolution. *Mater. Today* **2005**, *8*, 32–41.

(2) Gan, Y. Atomic and Subnanometer Resolution in Ambient Conditions by Atomic Force Microscopy. *Surf. Sci. Rep.* **2009**, *64*, 99–121.

(3) Binnig, G.; Quate, C. F.; Gerber, C. Atomic Force Microscope. *Phys. Rev. Lett.* **1986**, *56*, 930–933.

(4) Herruzo, E. T.; Asakawa, H.; Fukuma, T.; Garcia, R. Three-Dimensional Quantitative Force Maps in Liquid with 10 Piconewton, Angstrom and Sub-Minute Resolutions. *Nanoscale* **2013**, *5*, 2678–2685.

(5) Quate, C. F. The AFM as a Tool for Surface Imaging. *Surf. Sci.* **1994**, *299–300*, 980–995.

(6) Preiner, J.; Tang, J.; Pastushenko, V.; Hinterdorfer, P. Higher Harmonic Atomic Force Microscopy: Imaging of Biological Membranes in Liquid. *Phys. Rev. Lett.* **2007**, *99*, 046102–046105.

(7) San Paulo, A.; Garcia, R. High-Resolution Imaging of Antibodies by Tapping-Mode Atomic Force Microscopy: Attractive and Repulsive Tip-Sample Interaction Regimes. *Biophys. J.* **2000**, *78*, 1599–1605.

(8) Chen, X.; Davies, M. C.; Roberts, C. J.; Tendler, S. J. B.; Williams, P. M.; Burnham, N. A. Optimizing Phase Imaging via Dynamic Force Curves. *Surf. Sci.* **2000**, *460*, 292–300.

(9) Fukuma, T.; Kobayashi, K.; Matsushige, K.; Yamada, H. True Molecular Resolution in Liquid by Frequency Modulation Atomic Force Microscopy. *Appl. Phys. Lett.* **2005**, *86*, 193108–193110.

(10) Turner, R. D.; Kirkham, J.; Devine, D.; Thomson, N. H. Second Harmonic Atomic Force Microscopy of Living Staphylococcus Aureus Bacteria. *Appl. Phys. Lett.* **2009**, *94*, 043901.

(11) Payam, A. F.; Ramos, J. R.; Garcia, R. Molecular and Nanoscale Compositional Contrast of Soft Matter in Liquid: Interplay between Elastic and Dissipative Interactions. *ACS Nano* **2012**, *6*, 4663–4670.

(12) Assender, H.; Bliznyuk, V.; Porfyrakis, K. How Surface Topography Relates to Materials' Properties. *Science* **2002**, *297*, 973−976.
(13) Forchheimer, D.; Platz, D.; Tholén, E. A.; Haviland, D. B. Model-Based Extraction of Material Properties in Multifrequency Atomic Force Microscopy. *Phys. Rev. B* **2012**, *85*, 195449−195455.
(14) Herruzo, E. T.; Perrino, A. P.; Garcia, R. Fast Nanomechanical Spectroscopy of Soft Matter. *Nat. Commun.* **2014**, DOI: 10.1038/ncomms4126.
(15) Cartagena, A.; Raman, A. Local Viscoelastic Properties of Live Cells Investigated Using Dynamic and Quasi-Static Atomic Force Microscopy Methods. *Biophys. J.* **2014**, *106*, 1033−1043.
(16) Costa, L.; Rodrigues, M. S.; Newman, E.; Zubieta, C.; Chevrier, J.; Comin, F. Imaging Material Properties of Biological Samples with a Force Feedback Microscope. *J. Mol. Recognit.* **2013**, *26*, 689−693.
(17) Esteban-Ferrer, D.; Edwards, M.; Fumagalli, L.; Juárez, A.; Gomila, G. Electric Polarization Properties of Single Bacteria Measured with Electrostatic Force Microscopy. *ACS Nano* **2014**, *8*, 9843−9849.
(18) Pyne, A.; Thompson, R.; Leung, C.; Roy, D.; Hoogenboom, B. W. Single-Molecule Reconstruction of Oligonucleotide Secondary Structure by Atomic Force Microscopy. *Small* **2014**, *10*, 3257−3261.
(19) Weymouth, A. J.; Hofmann, T.; Giessibl, F. J. Quantifying Molecular Stiffness and Interaction with Lateral Force Microscopy. *Science* **2014**, *343*, 1120−1122.
(20) Fukuma, T.; Ueda, Y.; Yoshioka, S.; Asakawa, H. Atomic-Scale Distribution of Water Molecules at the Mica-Water Interface Visualized by Three-Dimensional Scanning Force Microscopy. *Phys. Rev. Lett.* **2010**, *104*, 016101−016104.
(21) Martinez-Martin, D.; Herruzo, E. T.; Dietz, C.; Gomez-Herrero, J.; Garcia, R. Noninvasive Protein Structural Flexibility Mapping by Bimodal Dynamic Force Microscopy. *Phys. Rev. Lett.* **2011**, *106*, 198101−198104.
(22) Israelachvili, J. *Intermolecular & Surface Forces*, 2nd ed.; Academic Press: New York, 1991.
(23) Preston, D. J.; Miljkovic, N.; Sack, J.; Enright, R.; Queeney, J.; Wang, E. N. Effect of Hydrocarbon Adsorption on the Wettability of Rare Earth Oxide Ceramics. *Appl. Phys. Lett.* **2014**, *105*, 011601.
(24) Bewig, K. W.; Zisman, W. A. The Wetting of Gold and Platinum by Water. *J. Phys. Chem.* **1965**, *69*, 4238−4242.
(25) Amadei, C. A.; Yang, R.; Chiesa, M.; Gleason, K. K.; Santos, S. Revealing Amphiphilic Nanodomains of Anti-Fouling Polymer Coatings. *ACS Appl. Mater. Interfaces* **2014**, *6*, 4705−4712.
(26) Baxamusa, S. H.; Gleason, K. K. Random Copolymer Films with Molecular-Scale Compositional Heterogeneities That Interfere with Protein Adsorption. *Adv. Funct. Mater.* **2009**, *19*, 1−8.
(27) Amadei, C. A.; Lai, C.-Y.; Heskes, D.; Chiesa, M. Time Dependent Wettability of Graphite upon Ambient Exposure: The Role of Water Adsorption. *J. Chem. Phys.* **2014**, *141*, 084709.
(28) Li, Z.; Wang, Y.; Kozbial, A.; Shenoy, G.; Zhou, F.; McGinley, R.; Ireland, P.; Morganstein, B.; Kunkel, A.; Surwade, S. P.; et al. Effect of Airborne Contaminants on the Wettability of Supported Graphene and Graphite. *Nat. Mater.* **2013**, *12*, 925−931.
(29) Lai, C.-Y.; Tang, T.-C.; Amadei, C. A.; Marsden, A. J.; Verdaguer, A.; Wilson, N.; Chiesa, M. A Nanoscopic Approach to Studying Evolution in Graphene Wettability. *Carbon* **2014**, *80*, 784−792.
(30) Pensini, E.; Yip, C. M.; O'Carroll, D. M.; Sleep, B. E. Effect of Water Chemistry and Aging on Iron—Mica Interaction Forces: Implications for Iron Particle Transport. *Langmuir* **2012**, *28*, 10453−10463.
(31) Garcia, R.; San Paulo, A. Attractive and Repulsive Tip-Sample Interaction Regimes in Tapping Mode Atomic Force Microscopy. *Phys. Rev. B* **1999**, *60*, 4961−4967.
(32) Sader, J. E.; Uchihashi, T.; Higgins, M. J.; Farrell, A.; Nakayama, Y.; Jarvis, S. P. Quantitative Force Measurements Using Frequency Modulation Atomic Force Microscopy—Theoretical Foundations. *Nanotechnology* **2005**, *16*, S94−S101.
(33) Katan, A. J.; van Es, M. H.; Oosterkamp, T. H. Quantitative Force Versus Distance Measurements in Amplitude Modulation AFM: A Novel Force Inversion Technique. *Nanotechnology* **2009**, *20*, 165703−165711.
(34) Santos, S.; Amadei, C. A.; Verdaguer, A.; Chiesa, M. Size Dependent Transitions in Nanoscale Dissipation. *J. Phys. Chem. C* **2013**, *117*, 10615−10622.
(35) Sader, J. E.; Jarvis, S. P. Accurate Formulas for Interaction Force and Energy in Frequency Modulation Force Spectroscopy. *Appl. Phys. Lett.* **2004**, *84*, 1801−1803.
(36) Tamayo, J. Energy Dissipation in Tapping-Mode Scanning Force Microscopy with Low Quality Factors. *Appl. Phys. Lett.* **1999**, *75*, 3569−3571.
(37) Basak, S.; Raman, A. Dynamics of Tapping Mode Atomic Force Microscopy in Liquids: Theory and Experiments. *Appl. Phys. Lett.* **2007**, *91*, 064107−064109.
(38) Santos, S.; Amadei, C. A.; Tang, T.-C.; Barcons, V.; Chiesa, M. Deconstructing the Governing Dissipative Phenomena in the Nanoscale. arXiv:1401.6587 [cond-mat.mes-hall], 2014.
(39) Butt, H.-J.; Jaschke, M. Calculation of Thermal Noise in Atomic I Force Microscopy. *Nanotechnology* **1995**, *6*, 1−7.
(40) Amadei, C. A.; Tang, T. C.; Chiesa, M.; Santos, S. The Aging of a Surface and the Evolution of Conservative and Dissipative Nanoscale Interactions. *J. Chem. Phys.* **2013**, *139*, 084708.
(41) Matlab and Simulink, R. A., The MathWorks, Inc., Natick Matlab and Simulink, Release 2010a, The MathWorks, Inc., Natick, 2010.
(42) Santos, S.; Guang, L.; Souier, T.; Gadelrab, K. R.; Chiesa, M.; Thomson, N. H. A Method to Provide Rapid in Situ Determination of Tip Radius in Dynamic Atomic Force Microscopy. *Rev. Sci. Instrum.* **2012**, *83*, 043707−043717.
(43) Maragliano, C.; Glia, A.; Stefancich, M.; Chiesa, M. Effective AFM Cantilever Tip Size: Methods for in-Situ Determination. *Meas. Sci. Technol.* **2014**, *26*, 015002.
(44) Santos, S.; Barcons, V.; Christenson, H. K.; Billingsley, D. J.; Bonass, W. A.; Font, J.; Thomson, N. H. Stability, Resolution, and Ultra-Low Wear Amplitude Modulation Atomic Force Microscopy of DNA: Small Amplitude Small Set-Point Imaging. *Appl. Phys. Lett.* **2013**, *103*, 063702−063705.
(45) Santos, S.; Thomson, N. H. Energy Dissipation in a Dynamic Nanoscale Contact. *Appl. Phys. Lett.* **2011**, *98*, 013101−013103.
(46) Ramos, J. Tip Radius Preservation for High Resolution Imaging in Amplitude Modulation Atomic Force Microscopy. *Appl. Phys. Lett.* **2014**, *105*, 043111−043114.
(47) Vahdat, V.; Grierson, D. S.; Turner, K. T.; Carpick, R. W. Mechanics of Interaction and Atomic-Scale Wear of Amplitude Modulation Atomic Force Microscopy Probes. *ACS Nano* **2013**, *7*, 3221−3235.